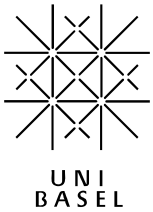

Temporal Photon Correlations in a One-Dimensional Atom

Master Project

Submitted by
Jannik Lukas Wyss

Supervisors
Dr. Marcelo Janovitch
Prof. Dr. Patrick Potts

University of Basel

December, 2025

1 Introduction

Photons do not easily interact with one another. To create useful correlations or entanglement, we rely on coupling to matter systems that mediate effective photon–photon interactions. These interaction-mediated effects underpin many photonic quantum technologies [1, 2].

In this work, we study the interaction of a single-mode coherent field with a two-level system inside a dissipative optical cavity. Such a cavity-atom system effectively realizes a one-dimensional atom, where light interacts with the emitter through a single spatial mode. Under appropriate conditions, this system can favor the emission of photon pairs over single photons, exhibiting photon-bundle emission, where one-photon states are suppressed [3, 4]. This bunching is mainly captured by Glauber's second-order coherence function $g^{(2)}$ [5].

This report refines the theoretical framework for a bad-cavity Jaynes–Cummings system under weak driving, focusing on the resulting signatures of photon-pair emission using waiting-time distributions. For the transmitted field of the two-sided cavity, our analysis confirms the previously reported strong photon bunching, but does not provide clear evidence that the bunching is dominated by strict two-photon emission. While the results are compatible with photon-pair emission, they do not allow us to rule out alternative multi-photon processes.

2 Driven Dissipative Jaynes–Cummings Model

2.1 Hamiltonian and Master Equation

We consider a two-level system (TLS) with transition frequency ω_a embedded in a single-mode cavity of frequency ω_c, formed by two semi-transparent mirrors with dissipation rates $\kappa_{L/R}$ (see Figure 1). The light-matter coupling strength is denoted by g, and the two-level system decays through an additional loss channel at rate γ. A coherent drive at frequency ω_d and amplitude ϵ is injected through the left mirror. The driven Jaynes-Cummings Hamiltonian reads

$$H = \underbrace{\Delta_c a^\dagger a}_{\text{cavity}} + \underbrace{\Delta_a \sigma^\dagger \sigma}_{\text{TLS}} + \underbrace{g(a^\dagger \sigma + \sigma^\dagger a)}_{\text{light-matter coupling}} - \underbrace{\sqrt{\kappa_L}\epsilon(a + a^\dagger)}_{\text{coherent drive}}, \tag{1}$$

where a and σ are the annihilation operators of the cavity mode and the two-level system, respectively, and $\Delta_c = \omega_c - \omega_d$ and $\Delta_a = \omega_a - \omega_d$ are detunings between the cavity/atom and the drive. Note that we use units such that $\hbar = 1$.

Photon loss through the mirrors and spontaneous emission are described by Lindblad dissipators, giving the master equation

$$\dot{\rho} = \mathcal{L}\rho = -i[H, \rho] + \kappa_L D[a]\rho + \kappa_R D[a]\rho + \gamma D[\sigma]\rho, \tag{2}$$

with $D[c]\rho = c\rho c^\dagger - \frac{1}{2}\{c^\dagger c, \rho\}$. Throughout this work, we use resonant conditions $\Delta_c = \Delta_a = 0$ and symmetric mirror rates $\kappa_R = \kappa_L$.

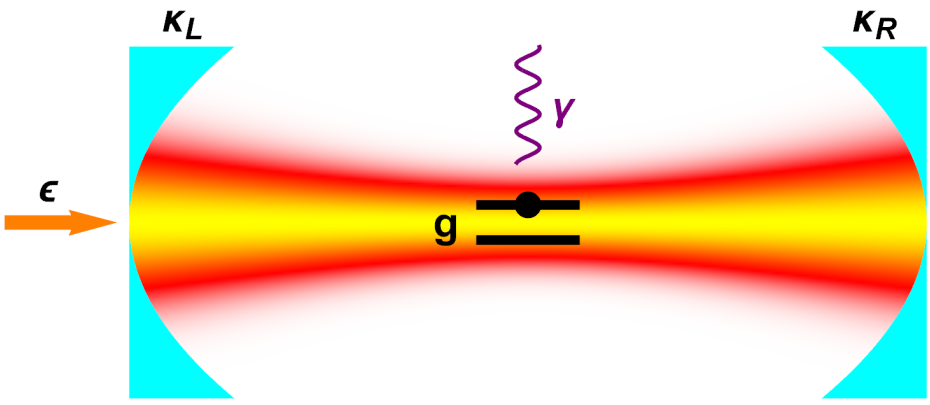

Figure 1: The driven-dissipative Jaynes-Cummings model consists of a two-level system coupled to a cavity mode. The cavity mirrors can leak photons with rates κ_L and κ_R, and the two-level system decays with rate γ. The light-matter coupling strength is denoted by g. A coherent drive at amplitude ϵ is injected from the left.

2.2 Cavity Characterization

To characterize the interplay of cavity parameters, we define the total decay rate $\kappa = \kappa_L + \kappa_R$ and the Purcell-enhanced decay $\Gamma = 2g^2/\kappa$. Their relation with the atomic loss γ is captured by the Purcell factor

$$F_P = \frac{4g^2}{\gamma\kappa}, \tag{3}$$

which, upon normalization, gives the coupling efficiency,

$$\beta = \frac{F_P}{F_P + 1} = \frac{4g^2}{4g^2 + \kappa\gamma}, \tag{4}$$

also known as the β-factor. It is the key quantity characterizing the one-dimensional atom [5].

2.3 Bad-Cavity & Weak-Drive Limit

In general, we work under the bad-cavity approximation where the excitation decays into the cavity before it is lost to the dissipative channel γ [6]. It is formalized with the dimensionless quantities

$$\frac{\gamma}{\kappa}, \frac{\gamma}{g}, \frac{\epsilon}{\sqrt{\kappa}} \ll 1. \tag{5}$$

We aim for a small number of input photons, which motivates operating in the weak-drive regime. This requires the input flux to be small compared to the smallest system parameter, which in the bad-cavity limit is γ,

$$\bar{n}_\gamma = \frac{\epsilon^2}{\gamma} \ll 1. \tag{6}$$

2.4 Adiabatic Elimination

The adiabatic elimination approximates the cavity field as adapting instantaneously to the two-level system, reducing the problem to the slower dynamics of the latter. This greatly simplifies the equations and allows for closed-form analytic solutions to the effective TLS dynamics.

2.4.1 Derivation of the Effective TLS-Only Dynamics

The starting point is the adjoint Liouvillian, which we define through

$$\frac{\mathrm{d}}{\mathrm{d}t}\langle A\rangle = \mathrm{tr}\Big\{A\,(\mathcal{L}\rho)\Big\} = \mathrm{tr}\Big\{(\mathcal{L}^\dagger A)\,\rho\Big\}, \qquad \text{so that} \qquad \dot{A} = \mathcal{L}^\dagger A. \tag{7}$$

With this relation, we can directly write down the Heisenberg equations for the two-sided cavity,

$$\begin{aligned}
\frac{\mathrm{d}}{\mathrm{d}t}a &= \mathcal{L}^\dagger a = i\sqrt{\kappa_L}\,\epsilon\,\mathbb{1} - \frac{\kappa}{2}a - ig\sigma,\\
\frac{\mathrm{d}}{\mathrm{d}t}\sigma &= \mathcal{L}^\dagger\sigma = -\frac{\gamma}{2}\sigma - ig\left(1 - 2\sigma^\dagger\sigma\right)a,\\
\frac{\mathrm{d}}{\mathrm{d}t}\sigma^\dagger\sigma &= \mathcal{L}^\dagger\sigma^\dagger\sigma = -\gamma\sigma^\dagger\sigma + ig\,(a^\dagger\sigma - \sigma^\dagger a).
\end{aligned} \tag{8}$$

To eliminate the cavity mode, we first solve the linear equation for $a(t)$ formally. This gives

$$a(t) = e^{-\frac{\kappa}{2}(t-t_0)}\left(a(t_0) - \frac{2i\sqrt{\kappa_L}\,\epsilon}{\kappa}\,\mathbb{1}\right) + \frac{2i\sqrt{\kappa_L}\,\epsilon}{\kappa}\,\mathbb{1} - ig\int_0^{t-t_0} du\, e^{-\frac{\kappa}{2}u}\,\sigma(t-u). \tag{9}$$

We assume $\frac{\kappa}{2}(t-t_0)$ is large enough such that we can neglect the first term and can extend the upper integral bound to infinity because the remaining part should be small because of the exponential decay. The integral converges absolutely because σ is bounded.

For the next approximation, we expand $\sigma(t-u)$ in a Taylor series around t, assuming that σ varies slowly on the cavity decay timescale. Substituting the series gives

$$\begin{aligned}
a(t) \approx \frac{2i\sqrt{\kappa_L}\,\epsilon}{\kappa}\,\mathbb{1} - ig\int_0^\infty du\, e^{-\frac{\kappa}{2}u}\,\sigma(t-u) &= \frac{2i\sqrt{\kappa_L}\,\epsilon}{\kappa}\,\mathbb{1} - ig\int_0^\infty du\, e^{-\frac{\kappa}{2}u}\sum_{n=0}^\infty \frac{(-u)^n}{n!}\frac{\mathrm{d}^n}{\mathrm{d}t^n}\sigma(t)\\
&= \frac{2i\sqrt{\kappa_L}\,\epsilon}{\kappa}\,\mathbb{1} - ig\sum_{n=0}^\infty (-1)^n\left(\frac{2}{\kappa}\right)^{n+1}\frac{\mathrm{d}^n}{\mathrm{d}t^n}\sigma(t).
\end{aligned} \tag{10}$$

By neglecting the higher-order terms in the sum, we obtain the adiabatic approximation for the cavity annihilation operator

$$a_{\mathrm{adb}} = \frac{2i\sqrt{\kappa_L}\,\epsilon}{\kappa}\,\mathbb{1} - ig\,\frac{2}{\kappa}\,\sigma(t) = \frac{2i\sqrt{\kappa_L}\,\epsilon}{\kappa}\,\mathbb{1} - i\sqrt{\frac{2\Gamma}{\kappa}}\,\sigma(t), \tag{11}$$

which is generally valid under the conditions

$$\frac{1}{\kappa t},\ \frac{g}{\kappa} \ll 1. \tag{12}$$

2.4.2 Applying the Effective Model

The elimination allows us to derive a linear equation for the TLS operators in the Heisenberg picture. Here we consider the two-sided cavity case with $\kappa_L = \kappa_R$ and obtain

$$\frac{\mathrm{d}}{\mathrm{d}t}\begin{pmatrix} \sigma^\dagger\sigma \\ \sigma \\ \sigma^\dagger \\ \mathbb{1} \end{pmatrix} = \underbrace{\begin{pmatrix} -\gamma-2\Gamma & \sqrt{\Gamma}\epsilon & \sqrt{\Gamma}\epsilon & 0 \\ -2\sqrt{\Gamma}\epsilon & \frac{1}{2}(-\gamma-2\Gamma) & 0 & \sqrt{\Gamma}\epsilon \\ -2\sqrt{\Gamma}\epsilon & 0 & \frac{1}{2}(-\gamma-2\Gamma) & \sqrt{\Gamma}\epsilon \\ 0 & 0 & 0 & 0 \end{pmatrix}}_{G} \underbrace{\begin{pmatrix} \sigma^\dagger\sigma \\ \sigma \\ \sigma^\dagger \\ \mathbb{1} \end{pmatrix}}_{\boldsymbol{\sigma}}. \tag{13}$$

This directly yields the steady-state averages,

$$\langle \boldsymbol{\sigma} \rangle_{ss} = \frac{1}{(\gamma+2\Gamma)^2 + 8\Gamma\epsilon^2} \begin{pmatrix} 4\Gamma\epsilon^2 \\ 2\sqrt{\Gamma}\epsilon(\gamma+2\Gamma) \\ 2\sqrt{\Gamma}\epsilon(\gamma+2\Gamma) \\ (\gamma+2\Gamma)^2 + 8\Gamma\epsilon^2 \end{pmatrix}. \tag{14}$$

Any operator O involving the cavity mode can be written in terms of the adiabatically eliminated cavity operator as $O(a, a^\dagger) \to O(a_{\mathrm{adb}}, a_{\mathrm{adb}}^\dagger) = \boldsymbol{c}^T\boldsymbol{\sigma}$, so the expectation value evaluates to $\langle O \rangle_\rho \approx \boldsymbol{c}^T \langle \boldsymbol{\sigma} \rangle_\rho$. For example, the steady-state intracavity photon number is given by

$$\langle n \rangle_{ss} \approx \langle a_{\mathrm{adb}}^\dagger a_{\mathrm{adb}} \rangle_{ss} = \frac{2}{\kappa}\left(\Gamma \langle \sigma^\dagger\sigma \rangle_{ss} - \sqrt{\Gamma}\epsilon \langle \sigma \rangle_{ss} - \sqrt{\Gamma}\epsilon \langle \sigma^\dagger \rangle_{ss} + \epsilon^2 \langle \mathbb{1} \rangle_{ss}\right) = \frac{2}{\kappa}\frac{\epsilon^2\left(\gamma^2 + 8\Gamma\epsilon^2\right)}{(\gamma+2\Gamma)^2 + 8\Gamma\epsilon^2}. \tag{15}$$

In the regime where the adiabatic elimination is valid (see Eq. 12), this expression agrees well with the numerical results. Outside this regime, however, clear quantitative and qualitative deviations appear, as shown in Fig. 2.

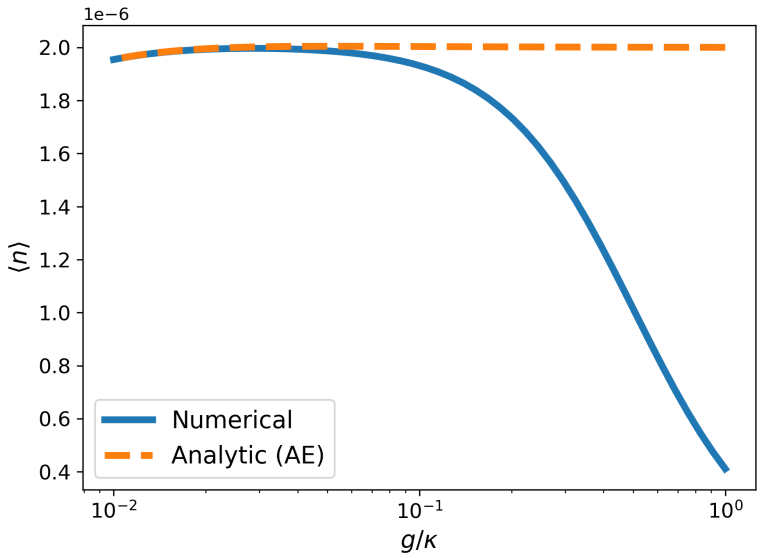

Figure 2: The steady-state intracavity photon number $\langle n \rangle$ as a function of the coupling ratio g/κ (logarithmic x-axis), comparing the full numerical solution of the master equation with the analytic result obtained from adiabatic elimination. The parameters are fixed to the dimensionless values $\gamma/g = 10^{-2}$ and $\epsilon^2/g = 10^{-3}$. The cavity decay rate κ is swept over two orders of magnitude. The curves agree in the regime $g/\kappa \ll 1$ but deviate once g becomes comparable to κ, illustrating the breakdown of the adiabatic-elimination approximation.

3 Photon Counting and Temporal Correlations

Unless stated otherwise, our treatment of photodetection, two-point current correlations, and waiting-time distributions closely follows Ref. [7].

3.1 Direct Photodetection

We describe photodetection events using classical random variables $dN(t) \in \{0, 1\}$, where $dN(t) = 1$ indicates that a jump occurred in the monitored channel, characterized by the jump operator L, during the infinitesimal interval $[t, t + dt]$. The increments $dN(t)$ update a counting process $N(t)$ that records how many detections have occurred up to time t. The statistics are determined as

$$P(dN(t) = 1 \,|\, \rho_c(t)) = dt \,\mathrm{tr}\big\{L^\dagger L\, \rho_c(t)\big\}\,, \tag{16}$$

which emphasizes that the jump probability at time t depends on the full conditional state $\rho_c(t)$ along the stochastic trajectory.

A click detector produces the stochastic photocurrent

$$I(t) = \frac{dN(t)}{dt}, \tag{17}$$

with expectation value

$$J(t) = \mathbb{E}[I(t)] = \mathrm{tr}\big\{L^\dagger L\, \rho(t)\big\}\,, \tag{18}$$

assuming ideal detection.

In this work, we only consider photodetection on the right-hand side output beam of the two-sided cavity, for which the jump operator is

$$L_R = \sqrt{\kappa_R}\, a. \tag{19}$$

3.2 Current Correlations and the Second-Order Coherence

Since $I(t)$ is a time series, we can study the correlations between fluctuations at different times, characterized by the two-point correlation function

$$F(t, t+\tau) = \mathbb{E}\big[I(t)I(t+\tau)\big] - J(t)J(t+\tau). \tag{20}$$

To describe the detection process, we consider the photon current associated with a single monitored decay channel, described by the jump operator L. The corresponding current $I(t)$ forms a point process of quantum jumps.

For quantum jumps, the two-point correlation function reads

$$\begin{aligned}\mathbb{E}[I(t)I(t+\tau)] &= \delta(\tau)J(t) + \mathrm{tr}\big\{\mathcal{J}\, e^{\mathcal{L}\tau}\, \mathcal{J}\, \rho(t)\big\} \\ &= \delta(\tau)J(t) + \langle L^\dagger(t) L^\dagger(t+\tau) L(t+\tau) L(t)\rangle,\end{aligned} \tag{21}$$

where $\mathcal{J}\rho = L\rho L^\dagger$ and we used the quantum regression theorem [8, 9].

In steady state, the two-point correlation function becomes a function only of the time difference τ and reduces to

$$F(\tau) = \delta(\tau)\, J + \langle L^\dagger(0) L^\dagger(\tau) L(\tau) L(0)\rangle_{\mathrm{ss}} - J^2 = \delta(\tau)\, J + J^2\big(g^{(2)}(\tau) - 1\big), \tag{22}$$

where

$$g^{(2)}(\tau) = \frac{\langle L^\dagger(0) L^\dagger(\tau) L(\tau) L(0)\rangle_{\mathrm{ss}}}{\langle L^\dagger L\rangle^2_{\mathrm{ss}}} = \frac{P\,(\,\mathrm{d}N(\tau) = 1 \mid \mathrm{d}N(0) = 1)}{P\,(\,\mathrm{d}N(0) = 1)}. \tag{23}$$

Given that a click occurred at $t = 0$, $g^{(2)}(\tau)$ quantifies how the conditional click rate at time τ compares to the steady-state rate [5].

3.3 Correlation and Bunching

In the context of quantum optics and photon detection, $g^{(2)}(\tau)$ becomes Glauber's second-order coherence function and quantifies delayed coincidences:

- **Correlation:** $g^{(2)}(\tau) > 1$ (or $F(\tau) > 0$) — a click at time t makes another click at delay τ more likely.
- **Anticorrelation:** $g^{(2)}(\tau) < 1$ (or $F(\tau) < 0$) - a click at time t suppresses the likelihood of another one at delay τ.

Because $g^{(2)}(\tau)$ is a smooth function, the value at zero delay already carries useful information, for example by updating the photon number conditioned on a click:

$$\langle a^\dagger a\rangle' = g^{(2)}(0)\,\langle a^\dagger a\rangle, \tag{24}$$

However, $g^{(2)}(0)$ alone does not uniquely characterize bunching. Non-monotonic curves can lead to situations where delayed coincidences dominate even if $g^{(2)}(0) < g^{(2)}(\tau)$ for some τ. To avoid such ambiguities, the following definitions are used:

- **Bunching:** $g^{(2)}(0) > g^{(2)}(\tau)$ for all τ - the maximum occurs at zero delay.
- **Antibunching:** $g^{(2)}(0) < g^{(2)}(\tau)$ for all τ - the minimum occurs at zero delay.

3.4 Waiting-Time Distribution

So far we have characterized photon statistics using current correlations and the second-order coherence function. A complementary and more time-resolved viewpoint is to consider the random delay between successive detection events. Specifically, we ask: given a click, what is the probability density for the time t until the next monitored jump? This defines the waiting-time distribution (WTD) [10, 11].

In systems with strongly correlated emission, such as photon-pair processes, the WTD can reveal characteristic features that are not captured by $g^{(2)}(\tau)$ alone. In particular, it can be sensitive to whether successive detections tend to occur in rapid succession followed by longer quiet periods, as one would expect if photons are emitted in pairs that are themselves separated in time.

To formalize this intuition, we describe the waiting-time distribution within the quantum-jump picture, where the dynamics consists of stochastic quantum jumps separated by periods of no-jump evolution. Suppose the system is in the steady state $\rho_{\rm ss}$ and a jump is registered in a monitored channel $q \in \mathcal{M}$, where $\mathcal{M}$ denotes the set of monitored Lindblad jump operators. The state is then updated according to

$$\rho_{\rm ss} \longrightarrow \rho_0 = \frac{\mathcal{L}_q \rho_{\rm ss}}{\mathrm{tr}\{\mathcal{L}_q \rho_{\rm ss}\}}, \tag{25}$$

where we define the jump superoperators

$$\mathcal{L}_q \rho = L_q \rho L_q^\dagger. \tag{26}$$

Between jumps, the state evolves under a conditional (no-jump) Liouvillian

$$\mathcal{L}_0 = \mathcal{L} - \sum_{q\in\mathcal{M}} \mathcal{L}_q, \tag{27}$$

which generates the non-unitary evolution corresponding to "no click" in any monitored channel. The waiting-time distribution for detecting a jump in channel k at time t after a jump in channel q is then

$$W(t, k \mid q) = \frac{\mathrm{tr}\big\{\mathcal{L}_k\, e^{\mathcal{L}_0 t}\, \mathcal{L}_q \rho_{\rm ss}\big\}}{\mathrm{tr}\{\mathcal{L}_q \rho_{\rm ss}\}}. \tag{28}$$

Thus, $W(t)\,dt$ is the probability that no monitored jump occurs up to time t and that the next jump occurs in the interval $[t, t+dt]$, i.e., it is the probability density for the delay between successive detection events.

The formalism extends naturally to sequences of multiple detection events. In particular, we may ask for the waiting time until the next click given that two jumps have already occurred. More generally, the probability density for observing a jump in channel k at time t after two preceding jumps in channels q_1 and q_2 is given by

$$W_2(t, k \mid q_2, q_1) = \frac{\mathrm{tr}\big\{\mathcal{L}_k\, e^{\mathcal{L}_0 t}\, \mathcal{L}_{q_2}\mathcal{L}_{q_1} \rho_{\rm ss}\big\}}{\mathrm{tr}\{\mathcal{L}_{q_2}\mathcal{L}_{q_1} \rho_{\rm ss}\}}. \tag{29}$$

As a probability density for the next detection event, the WTD must satisfy a basic consistency requirement, namely proper normalization. To obtain the waiting-time distribution for the next detection event irrespective of which monitored channel clicks, we sum over all monitored channels:

$$W(t \mid \rho_0) = \sum_{k\in\mathcal{M}} W(t, k \mid \rho_0) = -\,\mathrm{tr}\big\{\mathcal{L}_0 e^{\mathcal{L}_0 t}\rho_0\big\}\,, \tag{30}$$

where ρ_0 is the state after the inital jump. Defining the no-jump probability

$$P_{\rm no}(t \mid \rho_0) = \mathrm{tr}\big\{e^{\mathcal{L}_0 t}\rho_0\big\}\,, \tag{31}$$

we immediately obtain

$$W(t \mid \rho_0) = -\frac{d}{dt} P_{\mathrm{no}}(t \mid \rho_0), \tag{32}$$

and hence

$$\int_0^\tau W(t \mid \rho_0)\, dt = 1 - P_{\mathrm{no}}(\tau \mid \rho_0). \tag{33}$$

In the limit $\tau \to \infty$, we assume $P_{\mathrm{no}}(\infty \mid \rho_0) = 0$, i.e. the probability of never observing a jump vanishes. Numerically, Eq. (33) is a convenient diagnostic: deviations between the left- and right-hand sides directly reveal instabilities in the simulation.

3.5 Poisson Process

3.5.1 Single-Photon Emission

As a simple reference case, we consider completely uncorrelated photon detection. This corresponds to a Poisson counting process with constant rate λ.

The defining property of a Poisson process is that, in a short interval dt, the probability for a click is λdt, independent of the past. As a result, the probability to observe no click up to time t decays exponentially,

$$P_{\mathrm{no}}(t) = e^{-\lambda t}. \tag{34}$$

We want the waiting-time distribution from a photon detected at $t = 0$ to the next photon. It is given by the probability of no clicks up to time t, multiplied by the probability of a click in the next infinitesimal interval,

$$W(t)dt = P_{\mathrm{no}}(t)\lambda dt, \tag{35}$$

so that

$$W(t) = \lambda e^{-\lambda t}. \tag{36}$$

This exponential waiting-time distribution reflects the memoryless character of Poissonian emission [12]. The same absence of temporal correlations is expressed by the second-order coherence function,

$$g^{(2)}(\tau) = 1. \tag{37}$$

Deviations from either signature indicate non-Poissonian emission.

3.5.2 Photon-Pair Emission

We now consider an idealized point process in which emission events occur at Poisson-distributed times, but each event produces a photon pair. Pair start times T_k form a Poisson process with rate λ. Each pair emits two photons separated by a fixed delay $\delta > 0$, at times T_k and $T_k + \delta$.

We assume $\delta \ll 1/\lambda$, so that it is overwhelmingly unlikely to observe photons from different pairs within a time window of order δ. Under this assumption, if the detected photon is the first photon of a pair, the next photon is its partner, arriving after the fixed delay δ,

$$W_A(t) = \delta_D(t - \delta). \tag{38}$$

If the detected photon is the second photon of a pair, the next photon is the first photon of the next pair. Since pair start times are Poisson-distributed, the waiting time is exponentially distributed with rate λ,

$$W_B(t) = \lambda e^{-\lambda t}, \qquad t \geq 0. \tag{39}$$

Since both cases occur with equal probability, the total waiting-time distribution is

$$W(t) = \tfrac{1}{2}\delta_D(t - \delta) + \tfrac{1}{2}\lambda e^{-\lambda t}. \tag{40}$$

This waiting-time distribution consists of a sharp peak at $t = \delta$, reflecting the deterministic intra-pair delay, superimposed on an exponential tail that originates from the Poissonian timing of successive pairs. Figure 3 illustrates the exponential waiting-time distribution for a Poisson process, and contrasts it with a Poissonian pair-emission process.

The pair-emission process exhibits strong temporal correlations: photons are emitted in rapid succession within each pair, leading to pronounced zero-delay correlation,

$$g^{(2)}(0) \gg 1. \tag{41}$$

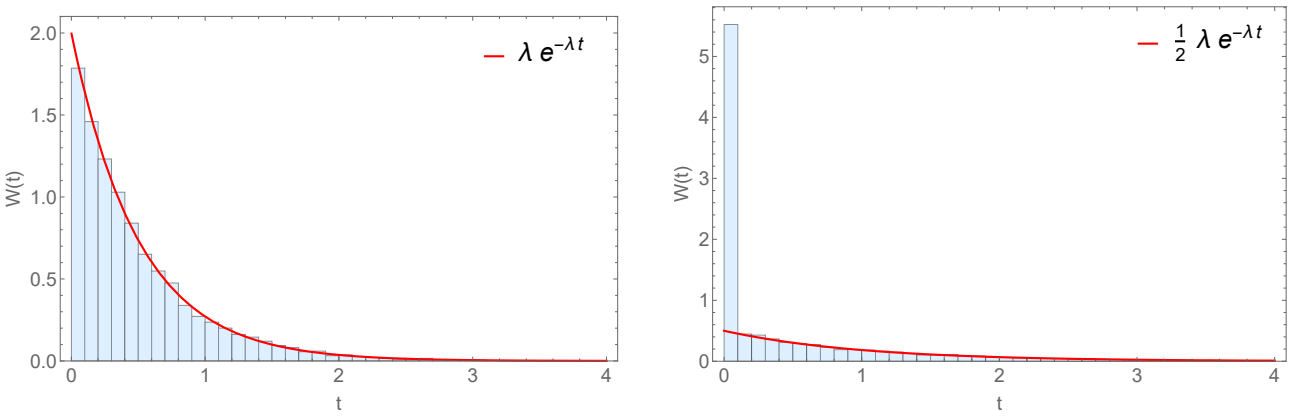

(a) Single-photon Poisson process

(b) Poissonian pair emission

Figure 3: Waiting-time distributions (blue histograms) obtained from Monte Carlo simulations of point processes. The red curves show the analytic exponential contributions. In the pair-emission case, half of all waiting times equal the fixed intra-pair delay $\delta = 0.001$, producing the sharp peak at $t = \delta$, while the remaining events form an exponential tail set by the inter-pair rate λ. For the single-photon Poisson process $\lambda = 2$, and for the pair-emission process $\lambda = 1$, chosen such that the total number of detected photons is approximately the same in both cases.

4 Results

4.1 Second-order Coherence Function

To characterize temporal intensity correlations of the transmitted field, we begin by computing the second-order coherence function $g^{(2)}(\tau)$. This quantity provides a direct diagnostic for photon bunching and antibunching. In the bad-cavity regime, closed-form analytic expressions for $g^{(2)}(\tau)$ are available [5], allowing us to validate the numerical implementation and to identify the parameter regime of strongest correlations. We therefore reproduce the analytic results and compare them to our fully numerical simulations.

Both the second-order coherence function and the waiting-time distribution are quantities conditioned on a detection event. Accordingly, the central object is the photon-conditioned state immediately after a click in the monitored output channel. For detection on the right side, this post-jump state is

$$\rho_0 = \frac{L_R \rho_{ss} L_R^\dagger}{\mathrm{tr}\{L_R^\dagger L_R \rho_{ss}\}}, \tag{42}$$

whose projection onto the operator basis gives the initial vector $\boldsymbol{\sigma}_0 = \langle \boldsymbol{\sigma} \rangle_{\rho_0}$. According to the quantum regression theorem, the subsequent evolution is governed by the same linear generator G from Eq. 13, so $\boldsymbol{\sigma}(\tau) = e^{G\tau}\boldsymbol{\sigma}_0$. For detection on the right side, the corresponding initial vector becomes

$$\boldsymbol{\sigma}_0 = \frac{\langle L_R^\dagger \boldsymbol{\sigma} L_R \rangle_{ss}}{\langle L_R^\dagger L_R \rangle_{ss}} = \frac{1}{r_{ss}} \begin{pmatrix} \epsilon^2 \langle \sigma^\dagger \sigma \rangle_{ss} \\ \epsilon^2 \langle \sigma \rangle_{ss} - \sqrt{\Gamma}\epsilon \, \langle \sigma^\dagger \sigma \rangle_{ss} \\ \epsilon^2 \langle \sigma^\dagger \rangle_{ss} - \sqrt{\Gamma}\epsilon \, \langle \sigma^\dagger \sigma \rangle_{ss} \\ r_{ss} \end{pmatrix}, \qquad r_{ss} = \mathrm{tr}\Big\{ L_R^\dagger L_R \rho_{ss} \Big\} = \kappa_R \langle a^\dagger a \rangle_{ss}, \tag{43}$$

Analogous to Eq. 15, we can approximate the second-order coherence function

$$g_R^{(2)}(\tau) = \frac{\boldsymbol{c}^T e^{G\tau} \boldsymbol{\sigma}_0}{r_{ss}}, \tag{44}$$

where $\boldsymbol{c} = \{\Gamma, -\sqrt{\Gamma}\epsilon, -\sqrt{\Gamma}\epsilon, \epsilon^2\}^T$. Thus, we obtain the intensity correlations for the transmitted light in the bad-cavity (Eq. 5) and weak-drive limit (Eq. 6),

$$\begin{aligned} g_R^{(2)}(\tau) &= \left[1 - \frac{\beta^2}{(1-\beta)^2} e^{-\gamma\tau/[2(1-\beta)]} \right]^2 + \mathcal{O}\left(\bar{\mathrm{n}}_\gamma\right), \\ g_R^{(2)}(0) &= \frac{(1-2\beta)^2}{(1-\beta)^4} + \mathcal{O}\left(\bar{\mathrm{n}}_\gamma\right). \end{aligned} \tag{45}$$

The full expression valid beyond the weak-drive limit is given in Appendix C, Eq. 68, and agrees with Ref. [5]. Note again that $g^{(2)}(\tau)$ is a smooth function, so its value at $\tau = 0$ already captures much of the relevant

behavior. The expression shows that a one-dimensional atom can, in principle, display both strong bunching ($\beta \approx 1$) and antibunching ($\beta = 1/2$).

We now compare these analytic predictions to fully numerical results. Throughout this work, unless stated otherwise, we choose parameters that satisfy the bad-cavity condition (Eq. 5), the weak-drive regime (Eq. 6), and the validity condition for adiabatic elimination $g \ll \kappa$ (Eq. 12). We focus in particular on large coupling efficiencies β, where strong photon correlations are expected.

Figure 4 shows $g^{(2)}(\tau)$ for the transmitted field. In the weak-drive regime, the numerical results are in good agreement with both the reduced analytic approximation (Eq. 45) and the full closed-form expression. In the strong-drive regime, the reduced analytic approximation fails. The curves show strong positive correlations at short times, followed by relaxation to the uncorrelated limit $g^{(2)}(\tau) \to 1$ for large τ. However, in the weak-drive regime there is anticorrelation at intermediate times.

The dependence of the zero-delay coherence on the drive strength is shown in Fig. 5. As ϵ increases, $g^{(2)}(0)$ decreases, indicating that the strongest bunching occurs in the weak-drive regime. As expected, the reduced approximation of Eq. 45 breaks down once the system is driven beyond this regime. Details of the numerical implementation and further consistency checks are given in Appendices E and F.

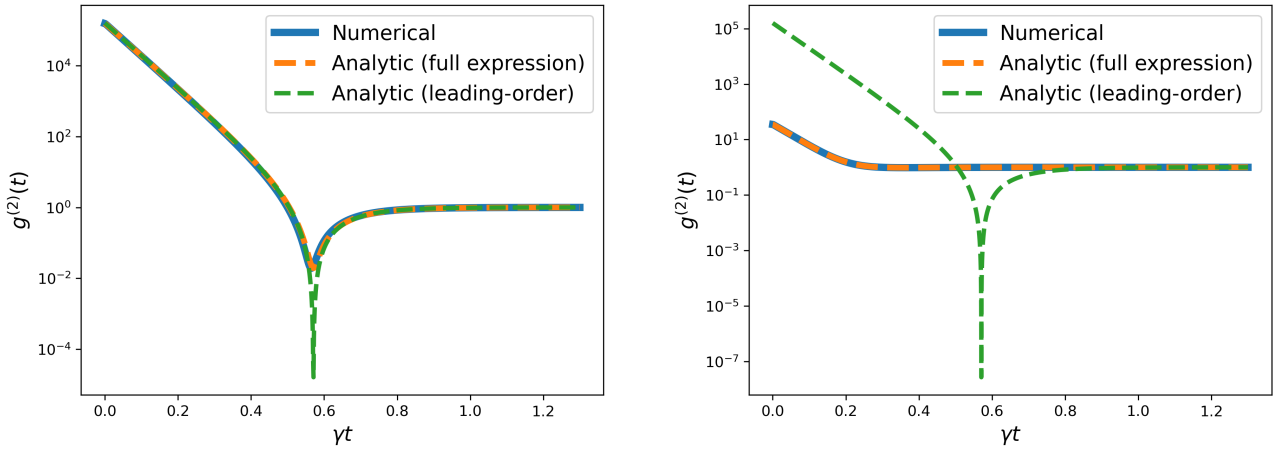

(a) Weak drive.

(b) Strong drive.

Figure 4: Second-order coherence function $g^{(2)}(\tau)$ for the right-going output field in the weak-drive (left, $\bar{n}_\gamma = 10^{-4}$) and strong-drive (right, $\bar{n}_\gamma = 1$) regimes, obtained from the fully numerical calculation and compared to two analytic expressions: a reduced approximation (Eq. 45) and the full closed-form result (Eq. 68). Time is rescaled by the decay rate γ. The parameters correspond to the dimensionless values $\gamma/g = 10^{-2}$, and $\kappa/g = 20$, giving a coupling efficiency $\beta \approx 0.95$.

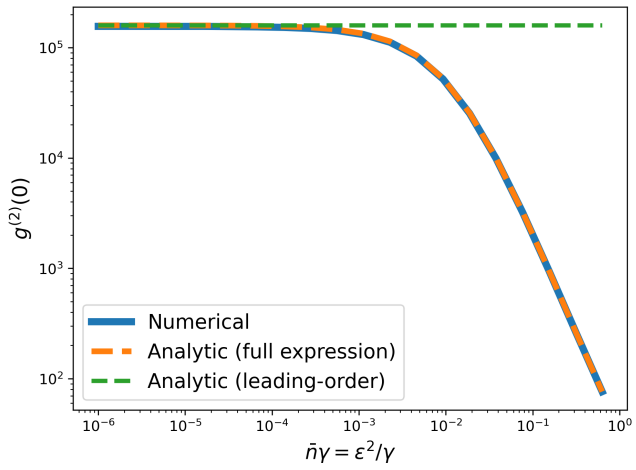

Figure 5: Second-order coherence $g^{(2)}(0)$ of the right–output field as a function of $\bar{n}_\gamma = \epsilon^2/\gamma$. Numerical steady-state results are compared to the analytic prediction of Eq. 68. Increasing ϵ reduces the zero-delay second-order coherence. The parameters correspond to the dimensionless values $\gamma/g = 10^{-2}$ and $\kappa/g = 20$, giving a coupling efficiency $\beta \approx 0.95$.

4.2 Fock State Populations

Given the strong bunching, one might expect multiphoton states to become more common inside the cavity while the single-photon state gets suppressed. A simple way to probe this is to push the weak-drive limit ($\langle n\rangle \ll 1$) to the extreme and truncate the photon number distribution at $n = 2$. We define

$$p_n := \langle n|\rho_{\mathrm{cav}}|n\rangle = \mathrm{tr}\left\{(|n\rangle\langle n| \otimes \mathbb{1})\,\rho_{\mathrm{ss}}\right\}, \tag{46}$$

where ρ_{ss} is the steady state of the full atom–cavity system and $\rho_{\mathrm{cav}} = \mathrm{tr}_{\mathrm{atom}}\{\rho_{\mathrm{ss}}\}$ its reduced cavity state.

In this truncated picture,

$$\langle n\rangle = \sum_n n\,p_n \approx p_1 + 2p_2, \qquad \langle n(n-1)\rangle = g^{(2)}(0)\,\langle n\rangle^2 = \sum_n n(n-1)\,p_n \approx 2p_2. \tag{47}$$

From these relations we obtain for the two-sided cavity

$$\begin{aligned} p_1 &\approx \langle n\rangle - g^{(2)}(0)\,\langle n\rangle^2 = \frac{(1-\beta)\,\beta\,\gamma}{2g^2}\,\epsilon^2 + \frac{\beta^2\epsilon^4}{4g^4}\left[8(2-\beta)\beta\,g^2 - \frac{(1-2\beta)^2\gamma^2}{(1-\beta)^2}\right] + O(\epsilon^6), \\ p_2 &\approx \tfrac{1}{2}\,g^{(2)}(0)\,\langle n\rangle^2 = \frac{(1-2\beta)^2\beta^2\gamma^2}{8(1-\beta)^2 g^4}\,\epsilon^4 + O(\epsilon^6). \end{aligned} \tag{48}$$

These expressions show that a high coupling efficiency β suppresses the leading-order (ϵ^2) contribution to the single-photon population p_1. Pushing β close to unity requires $4g^2 \gg \kappa\gamma$ which, together with the adiabatic-elimination condition $g \ll \kappa$ (Eq. 12), forces γ to be very small. In the limit $\gamma \to 0$ one finds

$$\lim_{\gamma\to 0} p_1 < \lim_{\gamma\to 0} p_2 \iff \kappa < \sqrt{3}g, \tag{49}$$

which is incompatible with $g \ll \kappa$. A more general calculation in Appendix D confirms that $p_1 < p_2$ cannot occur within the regime where the adiabatic model is valid. While zero-delay correlations in this truncated model only require $2p_2 > (p_1 + 2p_2)^2$, this still shows that the bunching cannot be interpreted as the cavity predominantly occupying the two-photon Fock state over the one-photon Fock state.

Figure 6 illustrates the resulting Fock state populations for parameters in the weak-drive and bad-cavity regime. For the large coupling efficiency $\beta \approx 0.95$, the zero-delay coherence $g^{(2)}(0) \sim 10^6$ (Eq. 45) indicates strong bunching. However, the cavity is still predominantly found in the single-photon state, with the two-photon population remaining smaller. This confirms the analytic conclusion that the observed bunching does not arise from the cavity preferentially occupying the two-photon Fock state.

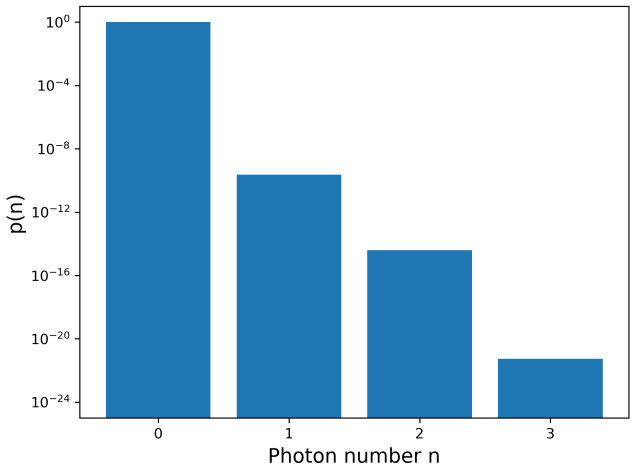

Figure 6: Fock state populations inside the two-sided cavity ($\kappa_L = \kappa_R$). The parameters correspond to the dimensionless values $\gamma/g = 10^{-2}$, $\epsilon^2/g = 10^{-6}$, and $\kappa/g \approx 20$, giving a coupling efficiency $\beta \approx 0.95$.

4.3 Waiting-Time Distribution

In the bunched regime, the detection of a photon strongly enhances the probability to detect another photon shortly thereafter. A natural question is whether this bunching reflects genuine photon-pair emission or merely short-time correlations within a broader emission process. To address this, we study the waiting-time distribution (WTD), which probes the full temporal structure of successive detection events.

If photons were predominantly emitted as well-separated pairs, one would expect a pronounced short-time peak corresponding to the second photon of a pair, followed by a second feature on longer time scales associated with the first photon of the next pair. The WTD therefore provides a more stringent test than $g^{(2)}(\tau)$ alone.

4.3.1 Analytical Approximation

For the waiting-time distribution, we evolve the system with the no-jump Liouvillian (see Eq. 27). We initially explored using the adjoint no-jump Liouvillian to obtain Heisenberg-like equations similar to Eq. 8, potentially allowing an approximation analogous to the adiabatic elimination. However, this approach fails because higher-order operator products such as $a^\dagger aa$ appear (see Appendix A).

We therefore proceed to use the original adiabatic elimination (Eq. 11) and derive the dynamics governed by the no-jump Liouvillian. This yields the linear system

$$\frac{\mathrm{d}}{\mathrm{d}t}\boldsymbol{\sigma} = \underbrace{\begin{pmatrix} -(\gamma+2\Gamma+\epsilon^2) & \sqrt{\Gamma}\epsilon & \sqrt{\Gamma}\epsilon & 0 \\ -\sqrt{\Gamma}\epsilon & -\frac{1}{2}(\gamma+2\Gamma+2\epsilon^2) & 0 & \sqrt{\Gamma}\epsilon \\ -\sqrt{\Gamma}\epsilon & 0 & -\frac{1}{2}(\gamma+2\Gamma+2\epsilon^2) & \sqrt{\Gamma}\epsilon \\ -\Gamma & \sqrt{\Gamma}\epsilon & \sqrt{\Gamma}\epsilon & -\epsilon^2 \end{pmatrix}}_{M}\boldsymbol{\sigma}. \tag{50}$$

Following the approach used for the $g^{(2)}$ function, we monitor the right port and write the waiting-time distribution as

$$W(t) = W(t, R \mid R) = \boldsymbol{c}^T e^{Mt}\boldsymbol{\sigma}_0, \tag{51}$$

where $\boldsymbol{c} = \{\Gamma, -\sqrt{\Gamma}\epsilon, -\sqrt{\Gamma}\epsilon, \epsilon^2\}^T$, and the time evolution is governed by M coming from the no-jump Liouvillian.

Apart from the matrix exponential, this expression can easily be evaluated analytically. To approximate the matrix exponential, we employ a Dyson series (see Appendix B)

$$e^{tM} = e^{tM_0} + \epsilon\int_0^t \mathrm{d}s\, e^{(t-s)M_0} M_D e^{sM_0} + \epsilon^2 \int_0^t \mathrm{d}s \int_0^s \mathrm{d}s' e^{(t-s)M_0} M_D e^{(s-s')M_0} M_D e^{s'M_0} + \mathcal{O}(\epsilon^3). \tag{52}$$

We retain the ϵ–dependent diagonal terms in M_0 so that the leading ϵt contributions stay inside the exponentials. The remaining off-diagonal terms are treated perturbatively. This choice significantly improves the short- and intermediate-time behavior, although the truncation inevitably breaks down at sufficiently long times. With this choice, we write

$$M = \underbrace{\begin{pmatrix} -\gamma-2\Gamma-\epsilon^2 & 0 & 0 & 0 \\ 0 & \frac{1}{2}\left(-\gamma-2\left(\Gamma+\epsilon^2\right)\right) & 0 & 0 \\ 0 & 0 & \frac{1}{2}\left(-\gamma-2\left(\Gamma+\epsilon^2\right)\right) & 0 \\ -\Gamma & 0 & 0 & -\epsilon^2 \end{pmatrix}}_{M_0} + \underbrace{\begin{pmatrix} 0 & \sqrt{\Gamma}\epsilon & \sqrt{\Gamma}\epsilon & 0 \\ -\sqrt{\Gamma}\epsilon & 0 & 0 & \sqrt{\Gamma}\epsilon \\ -\sqrt{\Gamma}\epsilon & 0 & 0 & \sqrt{\Gamma}\epsilon \\ 0 & \sqrt{\Gamma}\epsilon & \sqrt{\Gamma}\epsilon & 0 \end{pmatrix}}_{M_D}. \tag{53}$$

This allows the symbolic evaluation of the waiting-time distribution. The resulting closed-form expression is given in Appendix C, Eq. 70. Keeping all exponential factors intact while truncating higher-order prefactors consistent with the weak-drive regime yields

$$\begin{aligned} W(t) = {} & e^{-t\left(\frac{\gamma}{1-\beta}\right)} \frac{\beta^3\epsilon^2\left(\beta+(2-\beta)t\epsilon^2\right)}{(1-\beta)^2} \\ & + e^{-t\left(\frac{\gamma}{2-2\beta}\right)} 2\beta^2\epsilon^2\left(\frac{2(2-\beta)t\epsilon^2}{1-\beta} - 1\right) \\ & + e^{-t\epsilon^2}\left((1-\beta)^2\epsilon^2 + (2-\beta)\beta t\epsilon^4\right). \end{aligned} \tag{54}$$

It is normalized up to corrections of order $\mathcal{O}(\bar{n}_\gamma)$,

$$\int_0^\infty W(t)\,\mathrm{d}t = 1 + \mathcal{O}(\bar{n}_\gamma), \tag{55}$$

and reduces to the Poissonian waiting-time distribution (Eq. 39) in the uncoupled limit,

$$\lim_{g\to 0} W(t) = \epsilon^2 e^{-\epsilon^2 t}, \tag{56}$$

as expected (see Section 3.5.1). The normalization should, however, not be overinterpreted, as the approximate expression does not faithfully capture the long-time behavior of $W(t)$, as discussed in the next section.

4.3.2 Numerical Waiting-Time Distribution and Comparison

We now compare the analytic results to the full numerical WTD. We show three reference curves:

(i) the fully numerical WTD obtained from the exact no-jump evolution,

(ii) the analytic expression evaluated using the numerical matrix exponential (rather than the Dyson expansion), and

(iii) a reference WTD obtained by evolving the system from the ground state rather than from the post-detection state.

The latter is defined as

$$W_{\mathrm{re}}(t) = \mathrm{tr}\{\mathcal{L}_R\, e^{\mathcal{L}_0 t}\rho_{GS}\}\,, \qquad \rho_{GS} = |0\rangle\langle 0| \otimes |\downarrow\rangle\langle\downarrow|. \tag{57}$$

This construction corresponds to turning on the coherent drive at $t = 0$ and asking for the waiting time until the first detection event, rather than conditioning on a prior click. As such, it provides a genuinely memoryless starting point. We refer to this distribution as renewal, since the system is initialized in a fully reset state, from which the cavity field and TLS are rebuilt by the drive.

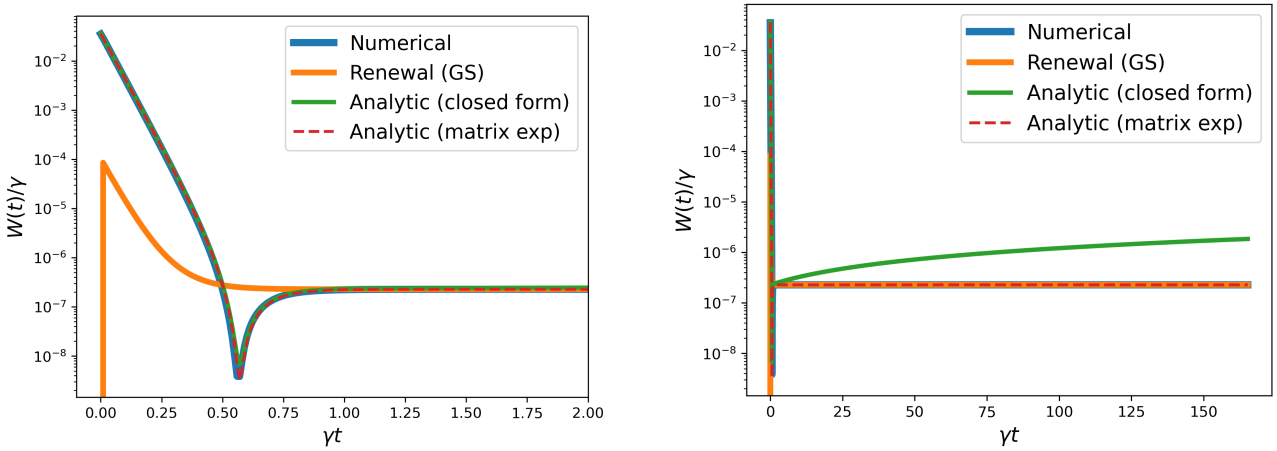

(a) Short-time behaviour.

(b) Extended-time behaviour.

Figure 7: Waiting-time distribution $W(\tau)$ for the right-going output field in the weak-drive regime ($\bar{n}_\gamma = 10^{-4}$), shown on short (left) and extended (right) time scales. Shown are the fully numerical WTD obtained from exact no-jump evolution, the analytic approximation evaluated using the numerical matrix exponential, the closed-form analytic expression, and a renewal reference WTD obtained by evolving from the ground state rather than the post-detection state. Time and probability density are rescaled by the decay rate γ. Parameters: $\gamma/g = 10^{-2}$, $\epsilon^2/g = 10^{-6}$, and $\kappa/g = 20$, corresponding to a coupling efficiency $\beta \approx 0.95$.

Figure 7 shows the WTD in the weak-drive regime ($\bar{n}_\gamma = 10^{-4}$) for a high coupling efficiency $\beta \approx 0.95$. Because the problem becomes numerically stiff at long times, the simulations do not directly access the full probability mass. However, fitting an exponential tail to the long-time numerical data (see Fig. 8) and adding the corresponding missing contribution yields a total probability very close to unity. This suggests that no additional late-time structure is missed and that the relevant dynamics are fully captured. Moreover, we verified our numerics in analytically solvable systems, as discussed in Appendix G, and found excellent agreement.

At short times, the WTD exhibits a peak immediately after a detection event, reflecting the strong enhancement of successive photon emission in the bunched regime. The distribution then dips and crosses over into an approximately exponential decay. Importantly, we do not observe a resolved second peak at longer times. Instead, the long-time behavior is well described by a single exponential. In this regime, the WTD approaches the corresponding renewal distribution, suggesting that the influence of the initial detection on later emission events becomes negligible.

As expected, the Dyson-series approximation deviates from the numerical result at longer times. In higher-order terms, the expansion parameter always appears in combination with powers of time ($t\epsilon^2$, $t^2\epsilon^4$, etc.), so that the truncation inevitably breaks down once t becomes sufficiently large. This limits the validity of the approximation to the short- and intermediate-time regime, where it nevertheless reproduces the numerical results well.

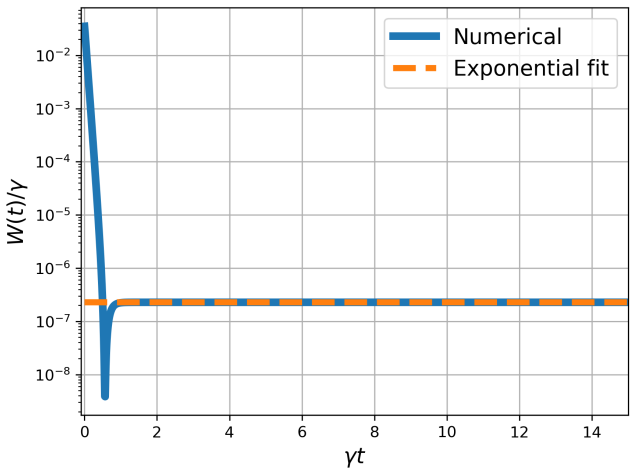

Figure 8: Waiting-time distribution $W(t)$ for the right-going output field in the weak-drive regime ($\bar{n}_\gamma = 10^{-4}$). The long-time tail ($\gamma t > \tau_{\max} = 5$) is fitted by an exponential $Ae^{-B\tau}$, capturing the asymptotic decay. Time and probability density are rescaled by the decay rate γ. Parameters: $\gamma/g = 10^{-2}$, $\epsilon^2/g = 10^{-6}$, and $\kappa/g = 20$, corresponding to a coupling efficiency $\beta \approx 0.95$. Integrating $W(\tau)$ numerically up to $\tau_{\max}$ yields a partial probability mass of 0.0017; including the fitted exponential tail gives a total normalization of $1 + 3 \times 10^{-6}$.

In the strong-drive regime ($\bar{n}_\gamma = 1$), shown in Fig. 9, the numerical integration captures almost the entire probability mass directly. The qualitative features largely persist: a strong short-time peak followed by an essentially exponential decay, again without evidence for a hypothesized secondary peak. However, no prominent dip at intermediate times is visible, consistent with the behavior observed in the second-order coherence function $g^{(2)}(\tau)$ (Fig. 4).

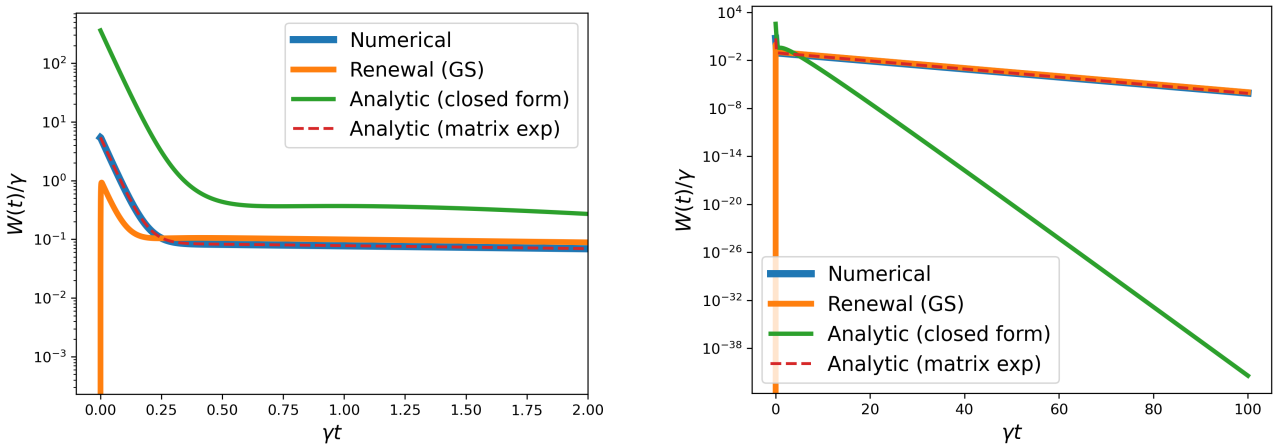

(a) Short-time behaviour.

(b) Extended-time behaviour.

Figure 9: Waiting-time distribution $W(\tau)$ for the right-going output field in the strong-drive regime ($\bar{n}_\gamma = 1$), shown on short (left) and extended (right) time scales. Shown are the fully numerical WTD obtained from exact no-jump evolution, the analytic approximation evaluated using the numerical matrix exponential , the closed-form analytic expression, and a renewal reference WTD obtained by evolving from the ground state rather than the post-detection state. Time and probability density are rescaled by the decay rate γ. Parameters: $\gamma/g = 10^{-2}$, $\epsilon^2/g = 10^{-2}$, and $\kappa/g = 20$, corresponding to a coupling efficiency $\beta \approx 0.95$.

4.3.3 Two-Click Waiting-Time Distribution $W_2(t)$

We now also consider the two-click waiting-time distribution $W_2(t)$ (Eq. 29), i.e., the probability density that, after two detections at $t = 0$ in the right output port, the subsequent detection occurs at time t. Since this corresponds to conditioning on a two-photon detection event, one might expect a delayed peak in the WTD in the case of well-separated pair emission. While we do not derive a full analytical approximation for $W_2(t)$, its zero-delay value $W_2(0)$ can be readily calculated using the adiabatic elimination (Eq. 11), and the resulting analytical prediction agrees well with the numerical simulations.

Figure 10 shows $W_2(t)$ for weak and strong driving. Consistent with the behavior of $W(t)$ in Figs. 7 and 9,

$W_2(t)$ does not exhibit a distinct late-time feature that would indicate sharply separated photon pairs; instead, it predominantly reflects short-time correlations followed by an approximately exponential relaxation.

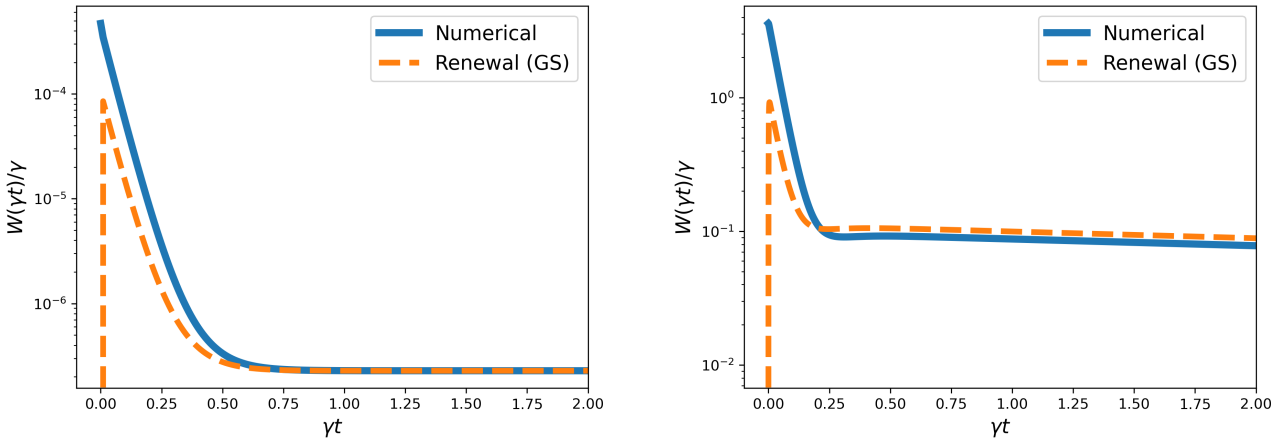

(a) Weak drive.

(b) Strong drive.

Figure 10: Two-click waiting-time distribution $W_2(\tau)$ for the right-going output field in the weak-drive (left, $\bar{n}_\gamma = 10^{-4}$) and strong-drive (right, $\bar{n}_\gamma = 1$) regimes. Shown are the fully numerical results and the renewal reference WTD obtained by evolving from the ground state rather than the post-detection state. Time and probability density are rescaled by the decay rate γ. Parameters: $\gamma/g = 10^{-2}$ and $\kappa/g = 20$, corresponding to a coupling efficiency $\beta \approx 0.95$.

5 Discussion

We reproduce the results for the second-order coherence function $g^{(2)}(\tau)$ reported in Ref. [5], which demonstrate strong bunching for large β factors in the bad-cavity and weak-driving regime. More precisely, we observe pronounced short-time temporal correlations between photon detections. At intermediate delays, the intensity correlations are suppressed and $g^{(2)}(\tau)$ drops below unity.

These intensity correlations below unity at finite delay cannot be explained by a classical stochastic process and instead require genuine quantum interference effects [5, 6]. In particular, while very strong bunching could in principle originate from thermal light, this interpretation can be ruled out if the correlations exhibit a subsequent dip below $g^{(2)}(\tau) = 1$ at later times [5], as observed here.

Motivated by these results, we turned to the waiting-time distribution (WTD) in an attempt to resolve individual photon pairs. If photons were emitted predominantly as well-separated pairs, one would expect two characteristic time scales to appear in the WTD: a short delay associated with the two photons within a pair, and a longer delay between successive pairs. In that case, the WTD would exhibit two distinct peaks. Instead, in the weak-drive regime we observe a single peak at zero delay followed by a dip and an approximately exponential relaxation, qualitatively mirroring the behavior of $g^{(2)}(\tau)$.

Importantly, the absence of a second peak does not rule out photon-pair emission. Our expectation relied on the assumption that pairs are well separated in time. However, as exemplified in Section 3.5.2, if photon pairs themselves are emitted according to Poissonian statistics with a fixed intra-pair delay, the resulting WTD exhibits only a single peak at the intra-pair delay followed by an exponential decay, without a second characteristic maximum. The same reasoning naturally extends to the two-click waiting-time distribution, which likewise does not develop a distinct second peak.

Finally, we do not observe an enhanced steady-state population of two-photon cavity states compared to the single-photon state.

In conclusion, while the waiting-time statistics do not provide new, unambiguous evidence for photon-pair emission, they also do not rule it out. Given the strong bunching observed in the weak-drive, bad-cavity regime and the fact that the system contains only a single two-level emitter and therefore cannot store multiple excitations, it remains highly plausible that the detected photons are predominantly emitted in pairs, albeit without a clear temporal separation that would make them directly resolvable in the waiting-time distribution.

References

[1] Kok, Pieter, W. J. Munro, Kae Nemoto, T. C. Ralph, Jonathan P. Dowling, and G. J. Milburn. "Linear Optical Quantum Computing with Photonic Qubits." Reviews of Modern Physics 79, no. 1 (2007): 135–74. https://doi.org/10.1103/RevModPhys.79.135.

[2] Chang, Darrick E., Vladan Vuletić, and Mikhail D. Lukin. "Quantum Nonlinear Optics — Photon by Photon." Nature Photonics 8, no. 9 (2014): 685–94. https://doi.org/10.1038/nphoton.2014.192.

[3] Tomm, Natasha, Sahand Mahmoodian, Nadia O. Antoniadis, et al. "Photon Bound State Dynamics from a Single Artificial Atom." Nature Physics 19, no. 6 (2023): 857–62. https://doi.org/10.1038/s41567-023-01997-6.

[4] Tomm, Natasha, Nadia O. Antoniadis, Marcelo Janovitch, et al. "Realization of a Coherent and Efficient One-Dimensional Atom." Physical Review Letters 133, no. 8 (2024): 083602. https://doi.org/10.1103/PhysRevLett.133.083602.

[5] M. Janovitch, *Fluctuations in the Quantum–to–Classical Frontier*, Inauguraldissertation, Philosophisch-Naturwissenschaftliche Fakultät, Universität Basel, 2025.

[6] Rice, P.R., and H.J. Carmichael. "Single-Atom Cavity-Enhanced Absorption. I. Photon Statistics in the Bad-Cavity Limit." IEEE Journal of Quantum Electronics 24, no. 7 (1988): 1351–66. https://doi.org/10.1109/3.974.

[7] Landi, Gabriel T., Michael J. Kewming, Mark T. Mitchison, and Patrick P. Potts. "Current Fluctuations in Open Quantum Systems: Bridging the Gap Between Quantum Continuous Measurements and Full Counting Statistics." PRX Quantum 5, no. 2 (2024): 020201. https://doi.org/10.1103/PRXQuantum.5.020201.

[8] Lax, Melvin. "Formal Theory of Quantum Fluctuations from a Driven State." Physical Review 129, no. 5 (1963): 2342–48. https://doi.org/10.1103/PhysRev.129.2342.

[9] Gardiner, Crispin W., and Peter Zoller. Quantum Noise: A Handbook of Markovian and Non-Markovian Quantum Stochastic Methods with Applications to Quantum Optics. Springer, 2000.

[10] Stratonovich, R. L. *Topics in the Theory of Random Noises*, Vol. 1. Gordon and Breach, Science Publishers, Inc., New York, 1963.

[11] Brandes, T. "Waiting Times and Noise in Single Particle Transport." Annalen Der Physik 520, no. 7 (2008): 477–96. https://doi.org/10.1002/andp.20085200707.

[12] Ross, Sheldon M. Introduction to Probability Models. Tenth edition. Academic Press, an imprint of Elsevier, 2010.

A Adjoint No-Jump Liouvillian

For the adiabatic elimination, we do

$$\frac{\mathrm{d}}{\mathrm{d}t}\langle A\rangle = \mathrm{tr}\Big(A\,\mathcal{L}\rho\Big) = \mathrm{tr}\Big((\mathcal{L}^\dagger A)\,\rho\Big), \qquad \text{so that} \qquad \dot{A} = \mathcal{L}^\dagger A. \tag{58}$$

Such that we could set $\mathcal{L}^\dagger a = 0$ and get $a = f(\sigma)$. We now briefly explore whether the adjoint of the no-jump conditioned Liouvillian $\mathcal{L}_0$ could allow for something similar. There, we can easily see

$$\mathrm{tr}\Big(A\,(\mathcal{L}_0\rho)\Big) = \mathrm{tr}\Big(A(\,\mathcal{L}\rho - \sum_{k\in\mathcal{M}}\mathcal{L}_k\rho)\Big) = \mathrm{tr}\Big((\mathcal{L}^\dagger A)\,\rho\Big) - \mathrm{tr}\Big(A\sum_{k\in\mathcal{M}}\mathcal{L}_k\rho)\Big) = \mathrm{tr}\Big((\mathcal{L}_0^\dagger A)\,\rho\Big), \tag{59}$$

With

$$\mathrm{tr}\Big(A(\mathcal{L}_k\rho)\Big) = \mathrm{tr}\Big(AL_k\rho L_k^\dagger\Big) = \mathrm{tr}\Big((L_k^\dagger A L_k)\rho\Big), \tag{60}$$

we obtain

$$\mathcal{L}_0^\dagger a = \mathcal{L}^\dagger a - \sum_{k\in\mathcal{M}}\mathcal{L}_k^\dagger a, \tag{61}$$

where $\mathcal{L}_k^\dagger O = L_k^\dagger O L_k$. This allows us to get the following equations

$$\begin{aligned}
\mathcal{L}_0^\dagger \mathbb{I} &= -\kappa_R a^\dagger a,\\
\mathcal{L}_0^\dagger a &= -i\Delta_c a + i\sqrt{\kappa_L}\,\epsilon - ig\sigma - \frac{1}{2}(\kappa_L+\kappa_R)a - \kappa_R a^\dagger a a,\\
\mathcal{L}_0^\dagger \sigma &= -\frac{\gamma}{2}\sigma - ig\left(1-2\sigma^\dagger\sigma\right)a - i\Delta_a\sigma - \kappa_R a^\dagger a\sigma,\\
\mathcal{L}_0^\dagger \sigma^\dagger\sigma &= -\gamma\sigma^\dagger\sigma + ig\left(a^\dagger\sigma - \sigma^\dagger a\right) - \kappa_R a^\dagger\sigma^\dagger\sigma a.
\end{aligned} \tag{62}$$

The cubic terms do not allow us to do an adiabatic elimination like before.

B Dyson Series

To approximate the matrix exponential, we let $M = M_0 + \epsilon M_D$ and use the Dyson series, $U(t) := e^{tM}$, $U_0(t) := e^{tM_0}$. Then

$$\dot{U}(t) = (M_0 + \epsilon M_D)U(t), \qquad U(0) = \mathbb{I}. \tag{63}$$

We switch to the interaction picture: $V(t) := U_0(-t)U(t) = e^{-tM_0}U(t)$. Then

$$\dot{V}(t) = e^{-tM_0}(\epsilon M_D)e^{tM_0}V(t) = \epsilon\, M_D^I(t)\,V(t), \qquad V(0) = \mathbb{I}, \tag{64}$$

with $M_D^I(t) := e^{-tM_0}M_D e^{tM_0}$. We get the integral equation:

$$V(t) = \mathbb{I} + \epsilon\int_0^t \mathrm{d}s\, M_D^I(s)\,V(s), \tag{65}$$

which we can iterate to second order:

$$V(t) = \mathbb{I} + \epsilon\int_0^t \mathrm{d}s\, M_D^I(s) + \epsilon^2\int_0^t \mathrm{d}s\int_0^s \mathrm{d}s'\, M_D^I(s)M_D^I(s') + \mathcal{O}(\epsilon^3). \tag{66}$$

Transform back: $U(t) = U_0(t)V(t) = e^{tM_0}V(t)$. Using $M_D^I(s) = e^{-sM_0}M_D e^{sM_0}$, we obtain the approximation

$$e^{tM} = e^{tM_0} + \epsilon\int_0^t \mathrm{d}s\, e^{(t-s)M_0}M_D e^{sM_0} + \epsilon^2\int_0^t \mathrm{d}s\int_0^s \mathrm{d}s' e^{(t-s)M_0}M_D e^{(s-s')M_0}M_D e^{s'M_0} + \mathcal{O}(\epsilon^3). \tag{67}$$

C Full Expressions

C.1 Second-Order Coherence Function

The full expression of the $g^{(2)}$ function comes from Eq. 44 and is given by

$$\begin{aligned}
g_R^{(2)}(\tau_\mathrm{P}) = 1 + \frac{e^{-\frac{3}{4}\tau_\mathrm{P}}F_\mathrm{P}^2\gamma}{(1+F_\mathrm{P})\left(\gamma+4F_\mathrm{P}\epsilon^2\right)^2\Omega}\Big[&(1+F_\mathrm{P})\left(\left(F_\mathrm{P}^2-2\right)\gamma + 8F_\mathrm{P}\epsilon^2\right)\Omega\cosh\left(\tau_\mathrm{p}\Omega/4\right)\\
&-\left(\left(F_\mathrm{P}^3+F_\mathrm{P}^2+2F_\mathrm{P}+2\right)\gamma - 8F_\mathrm{P}\left(5+F_\mathrm{P}\right)\epsilon^2\right)\sinh\left(\tau_\mathrm{p}\Omega/4\right)\Big],
\end{aligned} \tag{68}$$

where we introduced

$$\tau_\mathrm{P} = (1+F_\mathrm{P})\,\gamma\tau, \qquad \Omega = \sqrt{1 - \frac{32F_\mathrm{P}\epsilon^2}{(1+F_\mathrm{P})^2\,\gamma}}. \tag{69}$$

C.2 Waiting-time Distribution

The full expression of the WTD comes from Eq. 51 and is given by

$$
\begin{aligned}
W(t) = \frac{1}{(\gamma+2\Gamma)^4\,(\gamma^2+8\Gamma\epsilon^2)}\Bigg[& \\
& 8\gamma\Gamma^2\epsilon^2 e^{-\frac{1}{2}t\left(\gamma+2\left(\Gamma+\epsilon^2\right)\right)}\Big(4\epsilon^4(3\gamma+4\Gamma)-\gamma(\gamma+2\Gamma)^2+4\epsilon^2(\gamma+2\Gamma)^2(t(\gamma+\Gamma)+1)\Big) \\
& +16\Gamma^2\epsilon^2 e^{-t\left(\gamma+2\Gamma+\epsilon^2\right)}\Big(\Gamma^2(\gamma+2\Gamma)^2+\epsilon^4\big(\gamma^2(\Gamma t-1)+\gamma\Gamma(3\Gamma t+2)+2\Gamma^2(\Gamma t+2)\big) \\
& \quad +\epsilon^2(\gamma+2\Gamma)\big(\gamma^2+\Gamma^2(3\gamma t+4)+\gamma\Gamma(\gamma t+3)+2\Gamma^3 t\big)\Big) \\
& +e^{-t\epsilon^2}\Big(\gamma^4\epsilon^2(\gamma+2\Gamma)^2+4\gamma\Gamma\epsilon^4(\gamma+2\Gamma)\big(3\gamma^2\Gamma t+\gamma^2(\gamma t+2)+2\Gamma^2(\gamma t-2)\big) \\
& \quad +16\Gamma^2\epsilon^6\big(\gamma^2(2\gamma t-5)+\Gamma^2(13\gamma t-4)+\gamma\Gamma(9\gamma t-10)+6\Gamma^3 t\big)\Big)\Bigg].
\end{aligned}
\tag{70}
$$

As expected, it fulfills

$$
\frac{2}{\kappa}\frac{W_{\text{approx}}(0)}{<n>} = g^{(2)}(0). \tag{71}
$$

D Fock State Distribution

Here we extend the analysis, to check whether it is possible that the first Fock state is less populated than the second one in the cavity. We set

$$
\kappa \to 1, g \to \delta, \gamma \to \delta^n, \epsilon^2 \to \delta^m \tag{72}
$$

with $\delta \ll 1$ and $n \ll m$ such that $\beta \to 1$ while

$$
\epsilon^2 \ll \gamma \quad \text{and} \quad g \ll \kappa. \tag{73}
$$

We check whether p_1 is larger than p_2:

$$
p_1 - p_2 \approx \frac{3\delta^{2n}}{2} - \frac{3\delta^{4n}}{32\delta^{m+2}+2\delta^{2n}} > 0, \tag{74}
$$

where we neglected higher order contributions, given $\delta \ll 1$.

While numerical prefactors have been omitted, this analysis shows that within the considered parameter regime the inequality $p_1 < p_2$ cannot be satisfied.

E Numerical Stability in `QuantumOptics.jl`

In this work we employ the `QuantumOptics.jl` Julia framework for open quantum dynamics. Since the systems considered involve very small parameters, a naive implementation can lead to numerical instabilities. We therefore discuss the main functions used and the role of their numerical settings.

E.1 Time Evolution with the Master Equation

A standard routine for simulating dynamics is `timeevolution.master`. It calls `OrdinaryDiffEqCore.solve` with default algorithm `OrdinaryDiffEqLowOrderRK.DP5()` (Dormand-Prince method). While many solver parameters can be adjusted, the most relevant for our purposes are the error tolerances. By default, the solver uses

$$
\texttt{reltol} = 10^{-6}, \qquad \texttt{abstol} = 10^{-8}. \tag{75}
$$

Because we work with extremely small numbers, it is necessary to adjust these tolerances. In adaptive step-size control, the local error estimate e_i for each component is scaled by a mixed absolute-relative tolerance. For a step from u_0 to u_1, the normalized residual is

$$
r_i = \frac{e_i}{\alpha + \delta\,\max(|u_{0,i}|, |u_{1,i}|)}, \tag{76}
$$

where α corresponds to the absolute tolerance `abstol` and δ to the relative tolerance `reltol`. A step is accepted if a suitable norm of r_i does not exceed one. The default is the root-mean-square (RMS) norm to combine the componentwise residuals. With N the dimension of the state vector, the step is accepted if

$$\|r\|_{\mathrm{RMS}} = \sqrt{\frac{1}{N}\sum_{i=1}^{N} r_i^2} \leq 1. \tag{77}$$

E.2 Steady-State Solvers

Three main functions are available to compute steady states:

`steadystate.master`, `steadystate.eigenvector`, `steadystate.iterative`.

The `master` function performs a direct time evolution, analogous to `timeevolution.master`, and terminates once a steady-state condition is met. After each step, the trace distance between successive states is evaluated,

$$\frac{D(\rho(t), \rho(t-\Delta t))}{\Delta t} < \varepsilon, \tag{78}$$

with Δt the last time step and ε the specified tolerance (default `tol` $= 10^{-3}$). If this criterion is satisfied, the current state is accepted as the steady state.

The `eigenvector` method determines the steady state as the eigenvector of the Liouvillian corresponding to eigenvalue zero. To identify this eigenvalue, the condition $|\lambda| <$ `tol` is used, with default `tol` $= 10^{-9}$. By default two eigenvalues are computed, and a warning is issued if more than one satisfies the condition. In the current implementation, the underlying ARPACK routine `eigs` does not provide a robust way to systematically improve precision; thus, the accuracy is effectively limited by the specified tolerance in `eigenvector`

Finally, the `iterative` method vectorizes the master equation into a linear system and applies an iterative solver, defaulting to `IterativeSolvers.bicgstabl!`. Convergence is controlled by absolute and relative tolerances, with defaults `abstol` $= 0$ and `reltol` $= \sqrt{\epsilon_{\mathrm{mach}}}$, where ϵ_{mach} is the machine epsilon. The iteration terminates once the residual norm satisfies

$$\|r_k\| \leq \max\big(\texttt{reltol} \cdot \|r_0\|,\ \texttt{abstol}\big),$$

where $\|r_0\|$ denotes the initial residual norm. The relative tolerance can be reduced to improve precision, albeit at the cost of more iterations.

While rescaling the Liouvillian might also help with small values, it generally is not enough as can be seen in the following section.

E.3 Second-order correlation function in the Two-Sided Cavity

We now illustrate stability issues in the two-sided cavity by looking at the steady-state second-order correlation

$$g^{(2)}_{\mathrm{ss}}(0) = \frac{\langle a^\dagger a^\dagger a a\rangle_{\mathrm{ss}}}{\langle a^\dagger a\rangle^2_{\mathrm{ss}}} = \frac{\langle n(n-1)\rangle_{\mathrm{ss}}}{\langle n\rangle^2_{\mathrm{ss}}}, \tag{79}$$

which becomes numerically unstable when weak driving and large cavity losses lead to a very small photon occupation $\langle n\rangle_{\mathrm{ss}} \ll 1$.

With the default parameters, the eigenvector and iterative solvers yield very different distributions of $g^{(2)}(0)$ when executed repeatedly, as shown in Fig. 11. Not only do the mean values differ, but the iterative solver in particular exhibits a huge spread across runs. The master solver, in contrast, produces a consistent result - but with the default tolerance its value is incorrect because the evolution is stopped too early.

Reducing the solver tolerances improves both accuracy and stability. For the iterative solver, the spread of values shrinks by orders of magnitude (see Fig. 11), and the mean approaches the physically correct result. The master solver converges reliably once the tolerances are lowered, giving consistent values across runs without statistical spread.

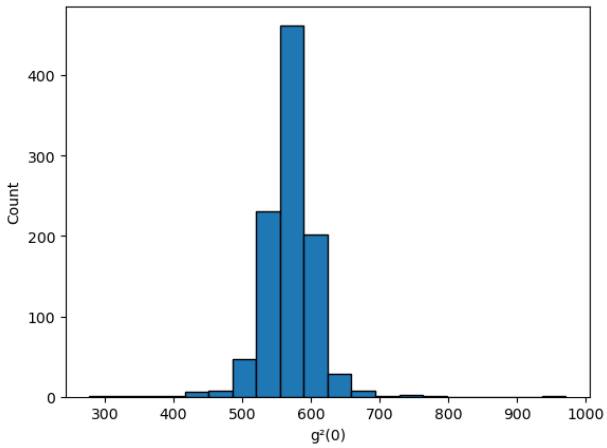

(a) Eigenvector (default): mean = 569.39, std = 39.43

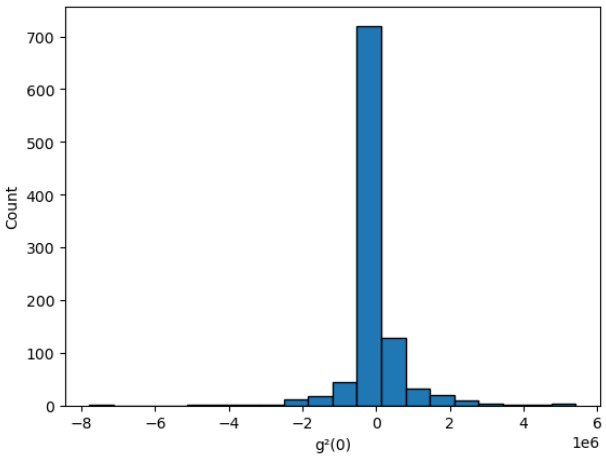

(b) Iterative (default): mean = 2.68×10^{4}, std = 7.81×10^{5}

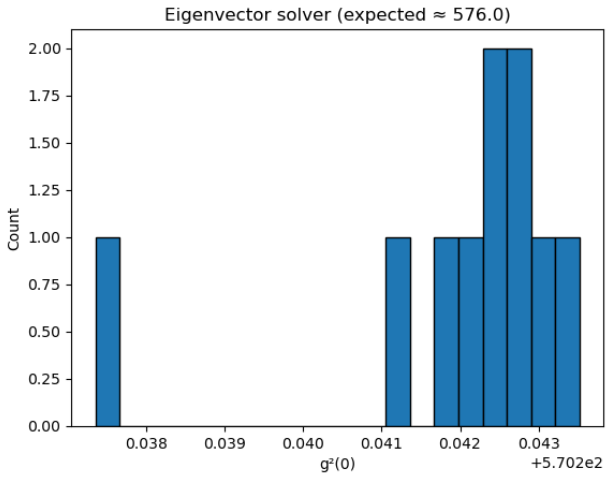

(c) Eigenvector (low tol): mean = 570.24, std = 1.71×10^{-3}

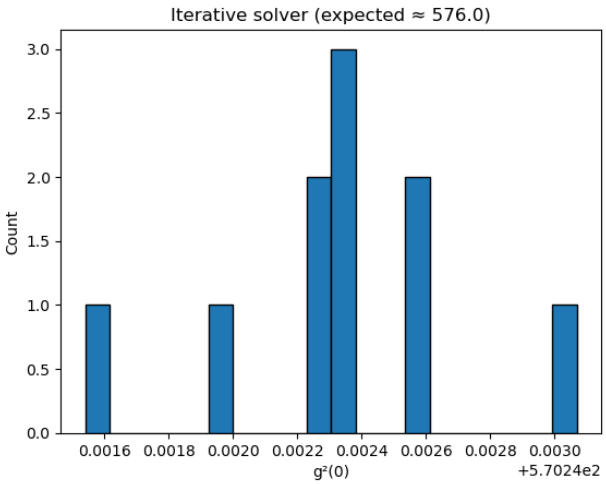

(d) Iterative (low tol): mean = 570.24, std = 3.94×10^{-4}

Figure 11: Steady-state $g^{(2)}(0)$ distributions obtained from eigenvector and iterative solvers with default and low tolerance parameters for the two-sided cavity master equation. Each histogram contains 1000 runs. Parameters: $\Delta_c = \Delta_a = 0.0$, $\gamma = 10^{-2}$, $\kappa_L = \kappa_R = 10.0$, $\varepsilon = 10^{-3}$, $g = 0.5$, and $N_{\text{cutoff}} = 3$.

The underlying reason for the instability is the amplification of small numerical errors by the denominator $\langle n\rangle^2$. If the solver returns $\rho_{\text{num}} = \rho + \delta\rho$, then

$$g^{(2)}_{\text{num}}(0) = \frac{\langle n(n-1)\rangle + \text{tr}[n(n-1)\delta\rho]}{(\langle n\rangle + \text{tr}[n\delta\rho])^2} = g^{(2)}(0) + \delta g. \tag{80}$$

To first order,

$$\delta g \approx \frac{\text{tr}[n(n-1)\,\delta\rho]}{\langle n\rangle^2} - \frac{2g^{(2)}(0)}{\langle n\rangle}\,\text{tr}[n\,\delta\rho]. \tag{81}$$

The $1/\langle n\rangle^2$ prefactor makes $g^{(2)}$ extremely sensitive: with $\langle n\rangle \sim 10^{-9}$, errors of order 10^{-11} in the moments can already shift $g^{(2)}$ by $O(10^7)$.

This sensitivity can also be seen directly from

$$\langle n(n-1)\rangle = \sum_n n(n-1)\,p_n, \tag{82}$$

with p_n the cavity state populations. Since p_0 dominates and higher-n populations are tiny, even small errors in $p_{n\geq1}$ (including unphysical negative values) are heavily amplified in $g^{(2)}$. This also explains the counterintuitive observation that increasing the Fock-space cutoff can worsen numerical stability.

To mitigate this, we enforce physicality of the numerical steady state by projecting onto the nearest valid density matrix (unit trace, positive semidefinite up to $\lambda < 10^{-14}$, and Hermitian). Combined with reduced tolerances, this yields consistent results with low standard deviation across all solvers and parameter regimes. Here we show the results with the parameters used in Figure 11:

Method	Mean	Std
Eigenvector	570.242	4.95×10^{-4}
Iterative	570.242	1.20×10^{-4}
Master	570.233	1.20×10^{-13}

Table 1: Comparison of steady-state solvers.

For the convergence condition of the master function, we used tol = 10^-10 and the other tolerances are

Solver	Absolute tolerance	Relative tolerance
Master equation	1×10^{-10}	–
Eigenvector	–	1×10^{-12}
Iterative	0	1×10^{-17}
Time evolution	1×10^{-18}	1×10^{-18}

Table 2: Numerical tolerances used for different solvers.

Because the master function consistently has the lowest spread and the mean coincides with the results of the other solvers, we use it for all calculations, enhancing reproducibility.

F Analytical Consistency Checks

I use a couple of analytical approximations to check my numerical implementations.

F.1 Transmission and Reflection amplitudes

We consider the transmission and reflection amplitudes,

$$\begin{aligned} \mathfrak{t} &= i\sqrt{\frac{\kappa}{2}}\frac{\langle a\rangle}{\epsilon}, \\ \mathfrak{r} &= 1 + i\sqrt{\frac{\kappa}{2}}\frac{\langle a\rangle}{\epsilon}. \end{aligned} \tag{83}$$

The experimentally accessible quantities are transmission and reflection functions, $T = |t|^2$, $R = |r|^2$; they are connected to the average current in the photo-counting process. The averages are to be taken at steady-state $\langle a\rangle_{ss}$. In the bad-cavity limit,

$$\begin{aligned} T &= \left[1 - \frac{\beta}{1 + 4(1-\beta)\beta\bar{n}_\gamma}\right]^2 = (1-\beta)^2 + \mathcal{O}(\bar{n}_\gamma), \\ R &= \left[\frac{\beta}{1 + 4(1-\beta)\beta\bar{n}_\gamma}\right]^2 = \beta^2 + \mathcal{O}(\bar{n}_\gamma), \end{aligned} \tag{84}$$

and the last equalities highlight the weak-drive expansion. Figure 12 shows the transmission function obtained numerically together with the analytical weak-drive expression, demonstrating excellent agreement in the bad-cavity regime.

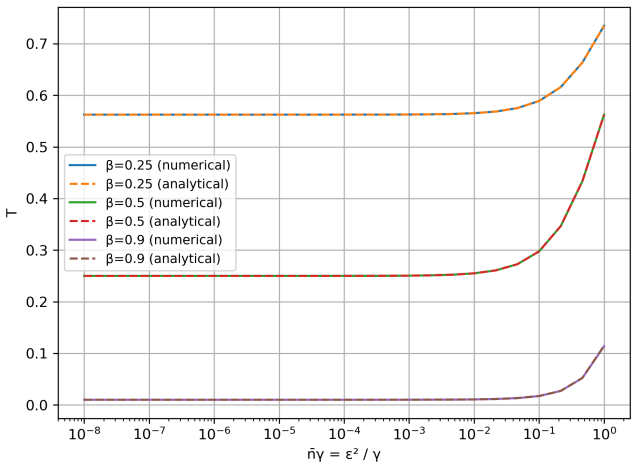

Figure 12: Transmission function of the two-sided cavity. The parameters are fixed to $\kappa_L/\gamma = \kappa_R/\gamma = 10^3$.

F.2 Intensity Correlations

For the light transmitted across the cavity,

$$g_R^{(2)}(\tau) = \frac{\langle a^\dagger a^\dagger(\tau) a(\tau) a \rangle_{\rm ss}}{\langle a^\dagger a \rangle_{\rm ss}^2}, \tag{85}$$

where we consider a delay between detection events, τ, and $t = 0$ denotes an arbitrary time at which the first detection happens and at which the system is assumed to be in the steady-state. In the bad-cavity limit, we get

$$\begin{aligned} g_R^{(2)}(\tau) &= \left[1 - \frac{\beta^2}{(1-\beta)^2} e^{-\gamma\tau/[2(1-\beta)]}\right]^2 + \mathcal{O}(\bar{n}_\gamma), \\ g_R^{(2)}(0) &= \frac{(1-2\beta)^2}{(1-\beta)^4} + \mathcal{O}(\bar{n}_\gamma). \end{aligned} \tag{86}$$

The corresponding second-order coherence function is shown in Fig. 13, where the numerical results agree with the analytical bad-cavity expression in the weak-drive regime.

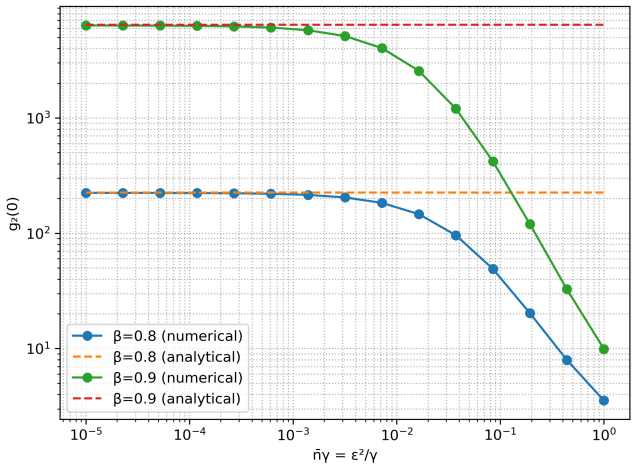

Figure 13: Second-order coherence function of the two-sided cavity. The parameters are fixed to $\kappa_L/\gamma = \kappa_R/\gamma = 10^3$.

G Analytical Waiting-time Distribution Examples

We now consider two analytically solvable two-level system dynamics, which serve as benchmarks for verifying our numerical implementation.

To recast the master equation in matrix form, we apply the vectorization identity

$$\mathrm{vec}(ABC) = (C^T \otimes A)\,\mathrm{vec}(B), \tag{87}$$

which maps the Liouvillian superoperator $\mathcal{L}$ to a matrix $\hat{\mathcal{L}}$ acting on the vectorized density matrix $\vec{\rho}$.

G.1 Example 1

As a first case, we study a driven two-level system with a single dissipative channel:

$$\dot{\rho} = -i[\Omega\sigma_x, \rho] + \gamma\, D[\sigma]\rho. \tag{88}$$

Using vectorization, one can directly obtain the steady state and, from it, the waiting-time distribution

$$W(t) = \frac{16\gamma\Omega^2 e^{-\frac{1}{2}(\gamma t)} \sinh^2\left(\frac{1}{4}t\sqrt{\gamma^2 - 16\Omega^2}\right)}{\gamma^2 - 16\Omega^2} \tag{89}$$

which reduces to $W(t) = 4t^2\Omega^3 e^{-2t\Omega}$ for $\gamma = 4\Omega$.

Defining $\delta = \sqrt{\gamma^2 - 16\Omega^2}$, we can distinguish between two damping regimes:

- If $\delta \in \mathbb{R}$ (overdamped), $W(t)$ has a single maximum.
- If δ is imaginary (underdamped), $W(t)$ exhibits infinitely many maxima.

This follows from the extrema condition

$$0 = \frac{\mathrm{d}}{\mathrm{d}t}W(t) = \frac{4\gamma\Omega^2 e^{-\frac{1}{2}\gamma t}\left(\gamma - \gamma\cosh\left(\frac{\delta t}{2}\right) + \delta\sinh\left(\frac{\delta t}{2}\right)\right)}{\delta^2}, \tag{90}$$

which simplifies to

$$\tanh\left(\tfrac{\delta t}{4}\right) = \frac{\delta}{\gamma}, \tag{91}$$

with solutions

$$t_k = \frac{4}{\delta}\left(\operatorname{arctanh}\left(\frac{\delta}{\gamma}\right) + i\pi k\right), \qquad k \in \mathbb{Z}. \tag{92}$$

Using $\operatorname{arctanh}(ix) = i\arctan(x)$ for real x makes the overdamped vs. underdamped distinction explicit. The numerical results match the analytical prediction, as seen in Fig. 14.

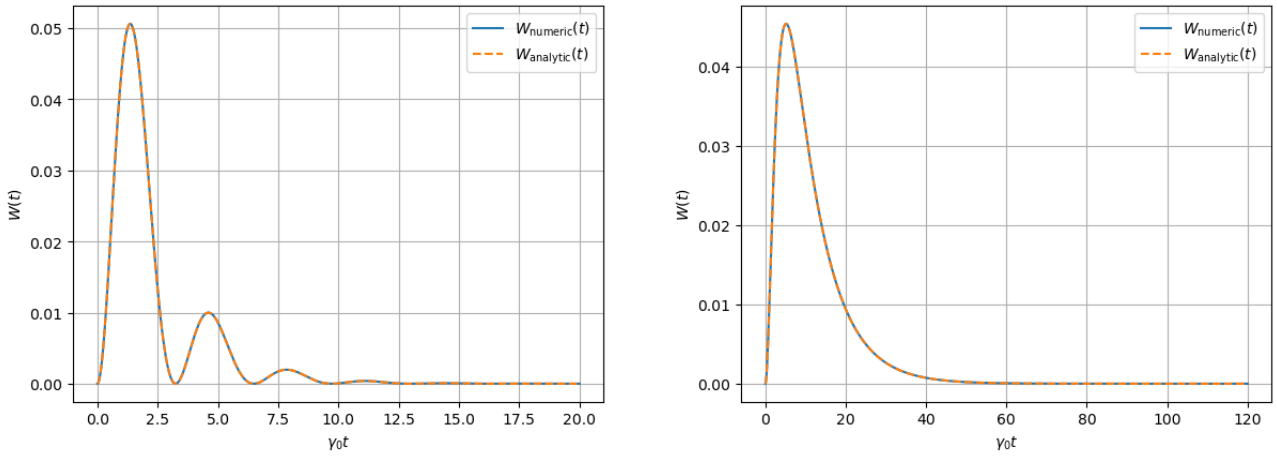

(a) Underdamped regime $\gamma_0 = 0.1$

(b) Overdamped regime $\gamma_0 = 0.6$

Figure 14: Waiting-time distributions for a driven two-level system with one dissipative channel. Driving strength is fixed at $\Omega = 0.1$.

G.2 Example 2

As a second case, we consider a two-level system with incoherent pumping and decay:

$$\dot{\rho} = \gamma_1 D[\sigma^\dagger]\rho + \gamma_2 D[\sigma]\rho. \tag{93}$$

This system is also solvable with vectorization, yielding

$$W(t) = \frac{\gamma_1\gamma_2\left(e^{-\gamma_1 t} - e^{-\gamma_2 t}\right)}{\gamma_2 - \gamma_1}, \tag{94}$$

which reduces to $W(t) = \gamma_1^2 t e^{-\gamma_1 t}$ for $\gamma_1 = \gamma_2$. Here no oscillatory behavior arises; the rates γ_1 and γ_2 simply determine the peak position

$$t_{\max} = \frac{\log\left(\frac{\gamma_1}{\gamma_2}\right)}{\gamma_1 - \gamma_2}. \tag{95}$$

The numerical results match the analytical prediction, as seen in Fig. 15.

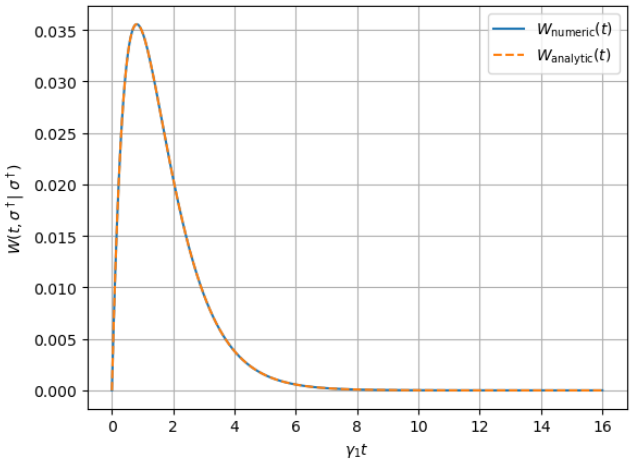

Figure 15: Waiting-time distribution for a two-level system with one pumped and one dissipative channel, monitoring the pumped channel. Parameters are $\gamma_1 = 0.08$ and $\gamma_2 = 0.12$.